

Quaternary sediment architecture in the Orkhon Valley (central Mongolia) inferred from capacitive coupled resistivity and Georadar measurements



Sonja Mackens^a, Norbert Klitzsch^b, Christoph Grützner^{c,*}, Riccardo Klinger^d

^a Geotomographie GmbH, Am Tonnenberg 18, Neuwied 56567, Germany

^b Applied Geophysics and Geothermal Energy, RWTH Aachen University, Aachen 52074, Germany

^c COMET, Department of Earth Sciences, University of Cambridge, Madingley Rise, Madingley Road, Cambridge CB3 0EZ, UK

^d Geolicious, Binzstr. 48, Berlin 13189, Germany

ARTICLE INFO

Keywords:

Ground penetrating radar
Capacitive coupled resistivity
Landscape evolution
Permafrost
Mongolia
Orkhon Valley

ABSTRACT

Detailed information on shallow sediment distribution in basins is required to achieve solutions for problems in Quaternary geology, geomorphology, neotectonics, (geo)archaeology, and climatology. Usually, detailed information is obtained by studying outcrops and shallow drillings. Unfortunately, such data are often sparsely distributed and thus cannot characterise entire basins in detail. Therefore, they are frequently combined with remote sensing methods to overcome this limitation. Remote sensing can cover entire basins but provides information of the land surface only. Geophysical methods can close the gap between detailed sequences of the shallow sediment inventory from drillings at a few spots and continuous surface information from remote sensing. However, their interpretation in terms of sediment types is often challenging, especially if permafrost conditions complicate their interpretation. Here we present an approach for the joint interpretation of the geophysical methods ground penetrating radar (GPR) and capacitive coupled resistivity (CCR), drill core, and remote sensing data. The methods GPR and CCR were chosen because they allow relatively fast surveying and provide complementary information. We apply the approach to the middle Orkhon Valley in central Mongolia where fluvial, alluvial, and aeolian processes led to complex sediment architecture.

The GPR and CCR data, measured on profiles with a total length of about 60 km, indicate the presence of two distinct layers over the complete surveying area: (i) a thawed layer at the surface, and (ii) a frozen layer below. In a first interpretation step, we establish a geophysical classification by considering the geophysical signatures of both layers. We use sedimentological information from core logs to relate the geophysical classes to sediment types. This analysis reveals internal structures of Orkhon River sediments, such as channels and floodplain sediments. We also distinguish alluvial fan deposits and aeolian sediments by their distinct geophysical signature. With this procedure we map aeolian sediments, debris flow sediments, floodplains, and channel sediments along the measured profiles in the entire basin.

We show that the joint interpretation of drillings and geophysical profile measurements matches the information from remote sensing data, i.e., the sediment architecture of vast areas can be characterised by combining these techniques. The method presented here proves powerful for characterising large areas with minimal effort and can be applied to similar settings.

1. Introduction

The shallow architecture of a sedimentary basin reflects the depositional geomorphic processes that occurred recently. These processes often interact or alternate with each other, and thus, the shallow sediment architecture can be highly complex. Braided river systems, for example, show a high spatial variability in sediment distribution caused by frequently changing river courses and by seasonal flooding events. Whereas braided river systems transport all grain sizes from clay to

gravel, aeolian processes deliver fine-grained material such as loess, and alluvial fans predominantly deposit gravel. The relative importance of those processes may vary over time, e.g., owing to climate variations, changes in base level, different sediment supply, vegetation, tectonic uplift or subsidence, or anthropogenic influence. This often results in a heterogeneous sediment distribution even in shallow depths.

Knowledge about the distribution of near-surface deposits in sedimentary basins is a prerequisite for many fields of research. For example, grain size distribution and layer thickness in the first couple of

* Corresponding author.

E-mail address: chg39@cam.ac.uk (C. Grützner).

<http://dx.doi.org/10.1016/j.geomorph.2017.05.002>

Received 2 January 2017; Received in revised form 3 May 2017; Accepted 3 May 2017

Available online 05 May 2017

0169-555X/ © 2017 Elsevier B.V. All rights reserved.

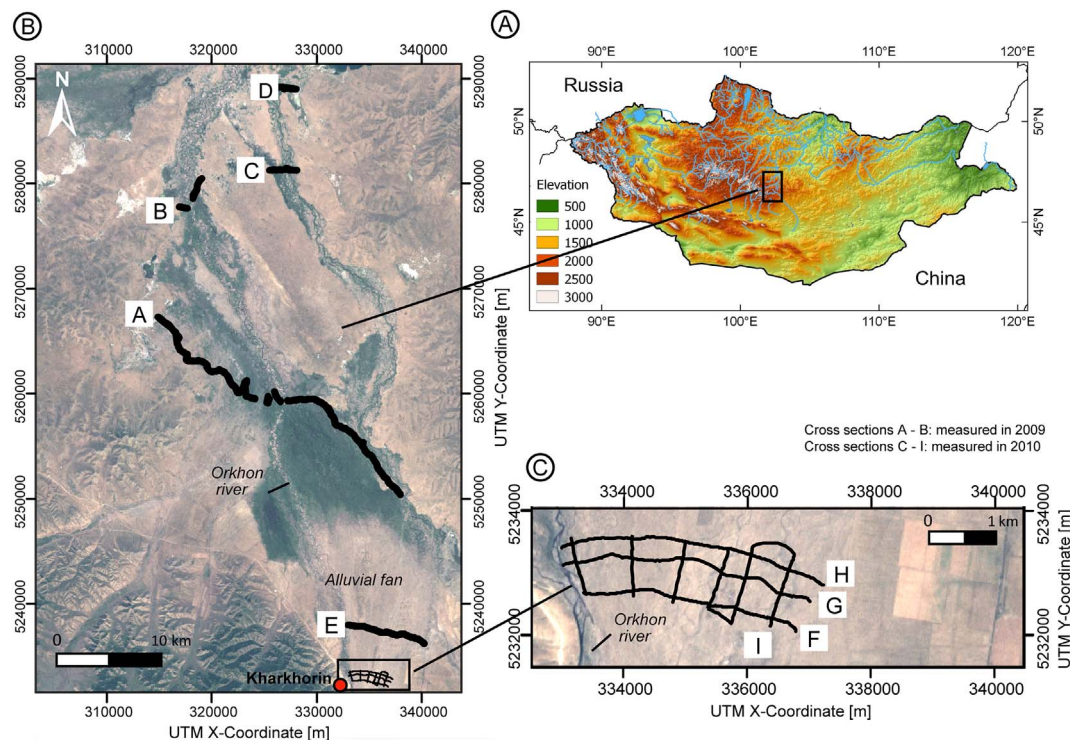


Fig. 1. Study site: (A) elevation map of Mongolia based on SRTM1 data (Gauss Krueger Projection), (B) satellite image (UTM projection) of the middle Orkhon Valley with geophysical cross sections A to E, and (C) detail of the study area with cross sections F to I.

metres are important parameters for groundwater studies, engineering, and environmental geology, as well as for permafrost research. Active tectonics can lead to a transient change in the location of deposition centres (e.g., basin tilting), which can be reconstructed when the shallow sediment distribution is known. The sedimentation history derived from present-day sediment distribution is used to address questions in geomorphology and geoarchaeology. Data on past river courses and fine-grained fertile soils can help to locate ancient settlements, and changes in the depositional environment often allow conclusions on human impact on the landscape. The latter motivated this study.

Imaging the distribution of near-surface deposits in sedimentary basins comes along with a number of difficulties. Outcrops and drill cores are often sparsely distributed and provide only one dimension or very local information. Thus, they do not record the spatial variability of the sediments in the entire basin. Moreover, the occurrence of permafrost impedes shallow drillings. Although geophysical prospection has been proven useful to image the shallow subsurface, it is costly in terms of time and money because long profiles and high resolution are needed. Even worse, high-resolution seismic reflection and refraction data often lack the necessary resolution and long profiles are difficult to measure (Cserkés-Nagy and Sztanó, 2016). The latter also applies to electrical resistivity tomography (ERT) where short electrode distances are required for high resolution measurements. This makes long profiles very time consuming and limits the actually measured profile lengths (Hilbich et al., 2008; Pellicer and Gibson, 2011; Rey et al., 2013; Grygar et al., 2016). Ground penetrating radar (GPR) reaches a very high spatial resolution and can be applied for long transects, but a shallow groundwater table and the presence of fine-grained material limit penetration depth (Davis and Annan, 1976; Neal, 2004; Woodward and Burke, 2007; Pellicer and Gibson, 2011). Remote sensing studies allow covering large areas (Klinger et al., 2011) but provide information of the land surface only. Moreover, their interpretation is often ambiguous without additional information. Hence, a combination of different methods is much more promising than a single method alone (cf. Schrott and Sass, 2008; Hausmann et al., 2013; Rey

et al., 2013).

In this paper, we present a methodology for combining the geophysical methods GPR and capacitive coupled resistivity (CCR) with borehole information and remote sensing data. We exploit the respective strengths of each method and develop a joint interpretation procedure that allows characterising the shallow sediment inventory of a sedimentary basin.

We apply the joint interpretation approach to the middle Orkhon Valley in central Mongolia, which is in the focus of archaeological, geoarchaeological, and environmental research mainly for two reasons: (i) It has a unique settlement history. Archaeological studies prove that various cultures preferred this region as a settlement location since Palaeolithic times (Bemmann et al., 2011). Since then, the region has experienced a turbulent history and seen a number of empires rise and fall. (ii) From the time of the first settlement up to the present, environmental conditions in the Orkhon Valley have dramatically changed, for example, as a result of deforestation. Special emphasis of the research is placed on the anthropogenic and natural factors that have caused the landscape changes (Rösch et al., 2005; Schwanghart et al., 2008; Bemmann et al., 2014).

In the following, we briefly introduce the morphological and sedimentological characteristics of our study area where fluvial, alluvial, and aeolian processes interact and result in a very heterogeneous valley fill. Then we explain the climatic conditions, and we discuss ground temperature distribution. Subsequently, we describe the methodology in detail and explain how we determine geophysical units in the subsurface, which are characteristic for certain sedimentary facies. The results of the geophysical prospection are compared to information from drill cores and remote sensing data.

2. Study area and climatic conditions

The middle Orkhon Valley, at around 1400 m asl (above sea level), encompasses the region between 47°44' N to 47°13' N and 102°32' E to 102°53' E; it stretches for > 30 km in the N-S direction and is up to 15 km wide. We conducted geophysical measurements in the northern

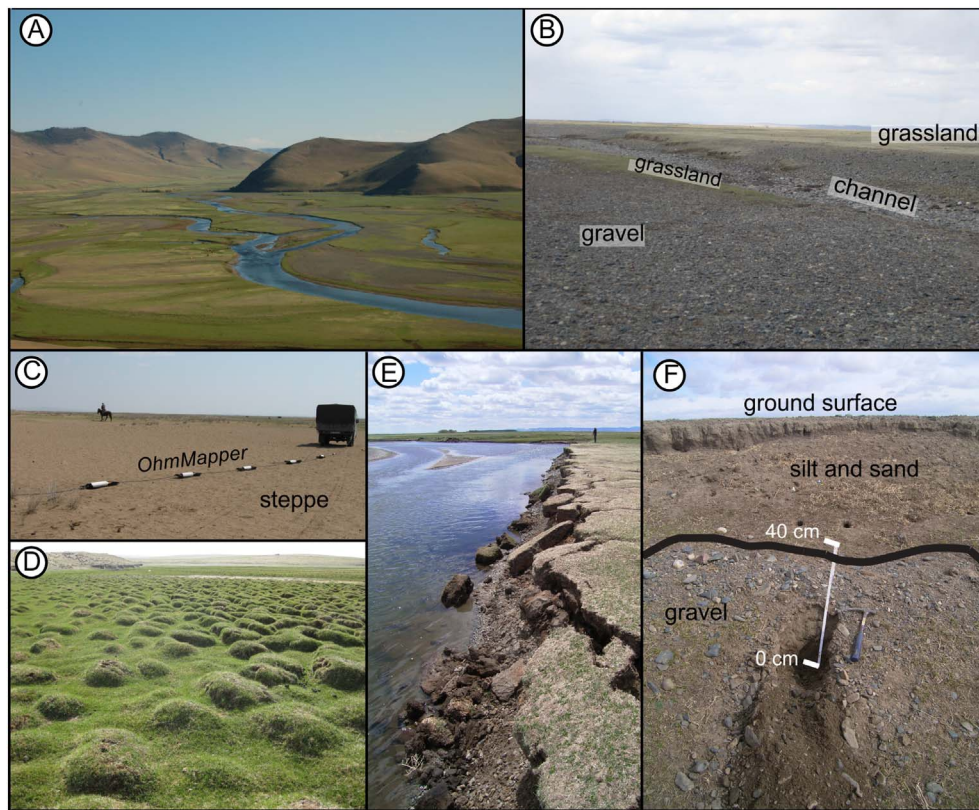


Fig. 2. Landscape characteristics of the study area: (A) Orkhon Valley (braided river system), (B) channel system of the alluvial fan, (C) OhmMapper being towed by vehicle in the steppe region, (D) hummocks, (E) river bank, and (F) exposure of sediments in the Orkhon Valley such as gravels, sand, and silt.

and southern parts of the middle Orkhon Valley (Fig. 1). The study area is part of the grassy steppe region of Mongolia (Fig. 2) with the Orkhon River (Fig. 2A) as the predominant feature. At the northern foot of the Khangai Mountains, where the Orkhon originates, the river valley widens to the middle Orkhon Valley. At the apex of a vast alluvial fan close to the study area, the medieval former Mongolian capital Karakorum (Kharkhorin) is located.

The present-day landscape is mainly influenced by the interaction of fluvial, glacial, and periglacial processes that occurred during the Quaternary and are still ongoing (Schwanghart and Schütt, 2008; Schwanghart et al., 2008; Bemmann et al., 2010; Lehmkuhl et al., 2011, 2012). Vast steppe regions (Fig. 2B, C) alternate with hummocky areas that testify to the permafrost conditions (Fig. 2D). Fluvial terraces flank the sides of the middle Orkhon Valley and intense river bank erosion is found (Fig. 2E). The Orkhon Valley is covered with thick deposits of Quaternary unconsolidated sediments. Well-rounded basaltic fluvial deposits that include rocks from a phase of middle to early Pleistocene volcanic activity and alluvial deposits alternate with loess and glacial loams rich in calcium carbonate (Fig. 2F; Schwanghart et al., 2008). The groundwater water table is relatively shallow, reaching a depth of < 2 m on the floodplain of the alluvial basin aquifer and increasing in the surrounding bedrock aquifer to a depth of < 10 m (Jadambaa et al., 2003; Martin, 2007).

According to the classification system of the International Permafrost Association (Brown et al., 1997) the Orkhon Valley is situated in the sporadic permafrost region (Fig. 3A). Therefore, the geophysical data are strongly influenced by the distribution of water and ice in the subsurface (Kneisel et al., 2008). A characteristic feature of permafrost soils is the active layer, which is the seasonally thawing and freezing top layer.

We conducted our field campaigns in May 2009 and May 2010 before the rain season when most of the annual precipitation occurs. In 2009, the frost period had already ended in March, and as a

consequence, the thawed layer reached greater depth than in 2010 when extraordinary cold prevailed up to late April. Actually, the winter of 2009/2010 was the coldest ever recorded in Mongolia. Precipitation in both years followed the mean annual pattern: 80 to 90% of the total annual precipitation of 65 mm occurs in the rain season between May and September when strong flood events frequently occur. Only up to 10% of the annual precipitation falls between November and May.

The temperatures in Tsetserleg (1693 m asl, 80 km west of study area; Fig. 3B) before and during the geophysical surveys in May 2009 and May 2010 are supposed to be representative for the temperature conditions in the study area. We used ground temperature profiles from a 7-m-deep borehole at the Nalaikh weather station (47°45' N, 107°20' E, 1421 m asl, 350 km east of the study area) for 2005 and 2006 as reference for ground temperatures (Fig. 3C). In 2009, the frost period ended in mid-March, similar to 2006, and about 50 days before our investigations. In 2010, the frost period lasted through the beginning of April, similar to 2005. Thus, the ground temperature curve from May 2005 is assumed to be representative for 2009, although the temperatures in 2009 were generally higher. According to these data, the thaw line is likely to be at about 1.8 m depth in 2009 and at about 0.8 m depth in 2010 (Fig. 3C). However, these depths are representative for the temperature history and soil type at the Nalaikh depression and are snapshots at a specific date. Therefore, they are only considered as rough estimates of the thaw line in the Orkhon Valley. Actually, the thaw line varies in space and time during the campaigns.

In the next section, we introduce the methods that we applied in this study, the obtained results, and our geophysical classification approach, i.e., the assignment of 'geophysical units'. Subsequently, the interpretation chapter shows how the ice and water content influence the geophysical data and how the geophysical units actually characterise the different sedimentological environments. Finally, we discuss our results and summarise the main findings of our study.

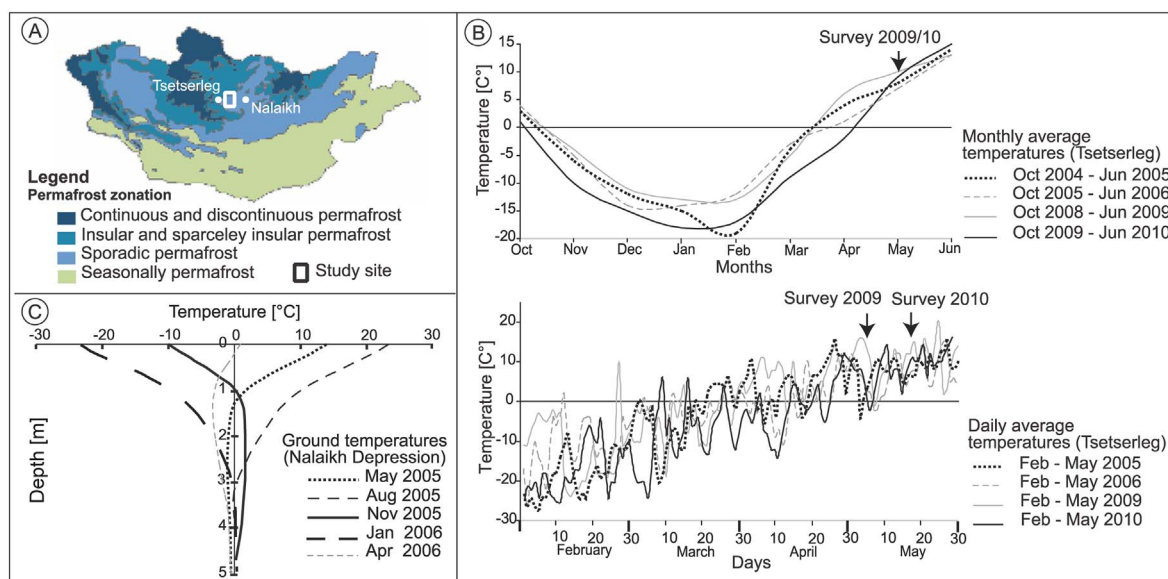


Fig. 3. (A) Map of permafrost distribution in Mongolia (after Sodnom and Yanshin, 1990) with indicated study site (white rectangle) in the area of sporadic permafrost. Note that this classification does not comply with the zonation by IPA (2017) which also reports sporadic permafrost in our study area; (B) monthly (top) and daily (bottom) average air temperatures in Tsetserleg (47°45' N, 101°47' E; 1693 m asl) from October to June and from February to May, respectively. The air temperatures are shown for the years 2005 and 2006 as well as for 2009 and 2010. (C) Ground temperatures measured in a 7-m-deep borehole at the Nalaikh Depression (47°45' N, 107°20' E, 1421 m asl; after Ishikawa et al., 2005).

3. Methods

We used ground penetrating radar (GPR) and capacitive coupled resistivity (CCR) to image the shallow subsurface sediment structure of the study area. Additionally, we took sediment cores at representative locations. Sediment analysis and electrical resistivity tomography have already been applied in the Ugi Nuur basin, central Mongolia, to investigate the sedimentary architecture of valley fillings (Schwanghart and Schütt, 2008), and elsewhere in Mongolia (Etzelmüller et al., 2006). The underlying physical principles and the data processing that was undertaken are explained below. Penetration depths of the geophysical measurements and the drillings did not exceed five metres.

The surveys were conducted along nine cross sections spanning the entire valley and with a total length of about 60 km (data see Mackens et al., 2011). Profiles A and B crossing the Orkhon River were measured in the first survey in May 2009. In a second survey in May 2010, measurements along profiles C to I were carried out (Fig. 1). The obtained resistivity distributions and GPR sections are interpreted up to a depth of about 3.5 m.

3.1. Ground penetrating radar (GPR)

Ground penetrating radar is widely used for sedimentological, glaciological, and ground ice investigations (Davis and Annan, 1976; Woodward and Burke, 2007). As a noninvasive geophysical technique, it images the shallow subsurface through the generation and detection of electromagnetic waves (e.g., Davis and Annan, 1989; Reynolds, 1997) exploiting their sensitivity to electric permittivity contrasts (Neal, 2004). Hence, GPR data can be utilised to infer sedimentological structures as long as they differ in permittivity. The soil permittivity is mainly influenced by water content (e.g., Topp et al., 1980) but also by the aggregate state of water (e.g., Daniels et al., 1995; Kneisel, 2006). This method is well suited to map vertical and horizontal profiles of frozen soil because of the high permittivity contrasts between ice and water (cf. Hinkel et al., 2001; Wu et al., 2009; Chen et al., 2016; Schennen et al., 2016; Table 1). Whereas the permittivity contrast controls the reflection of electromagnetic waves at interfaces, their attenuation depends on the electrical resistivity of the medium. The attenuation is high in thawed, water-rich soils and low in frozen ground. Thus, the penetration depth is closely related to thickness

Table 1

Resistivity, dielectric permittivity, thermal conductivity, and water retention (capillary rise) of materials relevant for this study (from Davis and Annan, 1989; Van Wijk and De Vries, 1963; Telford, 1990; Reynolds, 1997; Schick, 2002; Eppelbaum et al., 2014).

Material	Resistivity [Ωm]	Dielectric permittivity ϵ_r	Thermal conductivity [W/mK]	Water retention [cm]
Air [0 °C]	Insulating	1	0.024	–
Groundwater [0 °C]	10–300	88	0.6	–
Ice	10^3 – 10^6	3–4	2.38	–
Clay	1–100	5–40	0.25–1.58	> 400
Silt	1–1000	3–30	1.3–2.4	< 350
Sand	100–5000	4–30	0.3–2.2	20–100
Gravel	100–400	3–18	2.5–3.5	5–10

and water content of the thawed layer (Fig. 4).

We used a GPR system by GSSI (Geophysical Survey Systems Inc.) with a monostatic 270 MHz antenna. As there is a trade-off between penetration depth and resolution, we decided to use an intermediate-frequency antenna that, under favourable conditions, can penetrate down to 5 m and achieve a resolution in the order of 0.1 m. This resolution is needed to image fluvial sediment architecture.

The GPR data were processed with ReflexW (Sandmeier Scientific Software). Processing included (i) static correction, (ii) background removal, (iii) gain adjusting, (iv) average filtering, and (v) time-depth conversion. For the depth conversion of the GPR sections, velocities of 0.14 to 0.16 m/ns, deduced from a diffraction hyperbola analysis, were used.

3.2. Capacitive coupled resistivity (CCR)

Capacitive coupled resistivity is a geoelectrical method that provides a faster electrical resistivity survey than traditional direct current resistivity measurements (Timofeev, 1974; Kuras, 2002). Unlike conventional electrodes planted into the ground, CCR systems consist of a transmitter and a set of receiver antennas that are capacitively coupled to the ground. In our case, we used the OhmMapper (Geometrics Inc.) with five receiver dipoles. The antenna array is arranged in a single line and pulled along the ground either by a person or a vehicle (Fig. 2C).

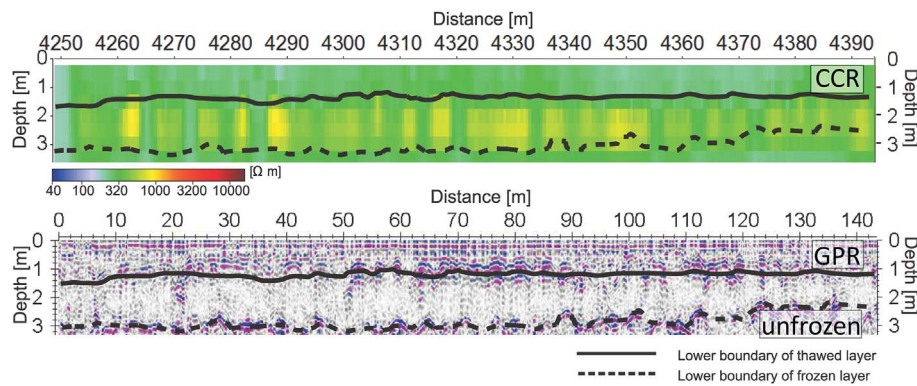


Fig. 4. The representative resistivity and GPR sections of the study area show the active layer (low resistivities, strong attenuation of GPR waves) above frozen soil (high resistivities, no reflections). The solid and the dashed lines mark the lower boundary of the active and the thin permafrost layer respectively. The sections show the same profile; they have different X-values (positions) because we recorded long CCR profiles and many short GPR profiles for technical reasons. See Fig. 6 for the location of the profile.

The main processing step for CCR data was the removal of measurement errors that occur as peaks within a smooth value distribution (despiking). Unfortunately, even after despiking our CCR data have a relatively high noise level. Therefore we chose to minimise the absolute changes in resistivity instead of the conventionally used square of difference between measured and calculated apparent resistivities in the inversion process. As no software is available for the inversion of line electrode data (to our knowledge), we used a DC resistivity inversion program (RES2DINV) for inverting the CCR data. We approximated the line electrode array by a four-point dipole–dipole geometry with a dipole length of 80% of the line electrodes according to Neukirch and Klitzsch (2010). A sensitivity analysis showed that using 80% of the CCR line electrode length as the virtual dipole length value minimises error in the inversion process. Although this method does not take into account the special line array geometry of the CCR system, Neukirch and Klitzsch (2010) found that a quantitative analysis of CCR data with this technique is possible and comparable to approaches that utilise more than one point substitute for each line electrode. Unless specialised software becomes available, this approach is the best practise to minimise inversion errors.

3.3. Shallow drillings

We used a percussion driller to obtain cores from up to 5 m depth at locations indicated by dots in Fig. 6. Core logs allow for determining soil type, grain size, sediment composition, and layer thicknesses (including frozen sediments). Since coarse-grained sediments cannot be penetrated by percussion drilling, investigation depths and the choice of drilling places are limited.

4. Geophysical results and their classification

In the following section, we explain our geophysical classification approach, which considers the geophysical signatures of both layers. The classification is based on (i) the electrical resistivity distributions, (ii) the structural patterns from GPR analysis, and (iii) the integration of lithological information derived from core log data. Finally, a sedimentological interpretation of the measured sections is given based on the geophysical classification and the lithological information obtained from drill cores.

Here, we show representative partitions of the geophysical sections (e.g., Figs. 4, 5, 7, 8, and 10). In general, our data indicate the presence of two distinct layers: a layer with lower resistivities above a surface-parallel layer with higher resistivities. The lower layer with resistivities between 150 and about 5000 Ωm and a thickness of about 1.5 m is observed in each resistivity profile. The upper boundary of this layer is frequently visible in GPR data in depths between 0.8 and 2 m. Some sections also show the lower boundary of the layer (Figs. 5 and 10).

These layers are interpreted as a thawed layer overlying a frozen layer. Because our measurements are snapshots in time only, we do not know whether or not parts of the soil are frozen throughout the entire year. We cannot differentiate between permafrost and seasonally frozen ground from our data. For this reason we use the terms ‘frozen layer’ and ‘thawed layer’ in the following.

4.1. Resistivity units

In a first step, we classify resistivity distributions derived from CCR measurements. For each campaign we assign five resistivity units RU I to RU V based on the resistivity values of these two distinct layers. In Fig. 5, resistivity units labelled RU I-1 to RU V-1 were assigned to resistivity sections measured in May 2009 in the northern part of the middle Orkhon Valley. Units labelled RU I-2 to RU V-2 refer to the investigation in May 2010, mostly in the southern part of the study area. The latter have higher resistivities than the 2009 units, especially in the frozen layer. This effect is a result of the different climatic conditions before and during the two campaigns (see also Section 2). The lower soil temperature, i.e., the higher amount of ice in the shallow subsurface in 2010, is responsible for the resistivity increase.

Fig. 6 illustrates the spatial distribution of resistivity units RU I to RU V. Resistivity units I, II, and IV dominate in the Orkhon Valley. Unit RU I occurs mainly on the east side of the Orkhon River in the floodplains (Fig. 6D) and near the northern Orkhon's tributaries (Fig. 6B). This unit is characterised by low resistivities in the thawed and frozen layers (Fig. 5). Unit RU II can be found predominantly west of the Orkhon River and in the southern part of the valley on the alluvial fan (Fig. 6D, E). Unit RU III occurs mainly in the central valley area west of the Orkhon River (Fig. 6D). Unit RU IV with high resistivities (Fig. 5) is found east of the Orkhon River (Fig. 6D and in the southern part of the valley (Fig. 6E). Unit RU V is characterised by the highest resistivities and occurs only in the west of the Orkhon River and in parts of the alluvial fan in the south (Fig. 6C, E).

4.2. Combining ground penetrating radar and resistivity data

In a second step, we use the additional information from GPR to refine the postulated RUs resulting into 18 geophysical units (GU), which are summarised in Fig. 10. Each RU is subdivided into several GUs (marked with lower case letters ‘a–c’) based on different GPR patterns and sedimentological data from drill cores.

Unit RU II-2 (measured in 2010) is taken as an example to illustrate the subdivision into GUs. Fig. 7 shows CCR sections of RU II-2 from two sites as well as the corresponding GPR sections. While the geoelectrical sections are similar, the GPR sections differ from each other. The GPR section of GU IIa-2 (Fig. 7A) is characterised by a more or less reflection-free pattern. Not only the thaw line at 1.5 m depth, inter-

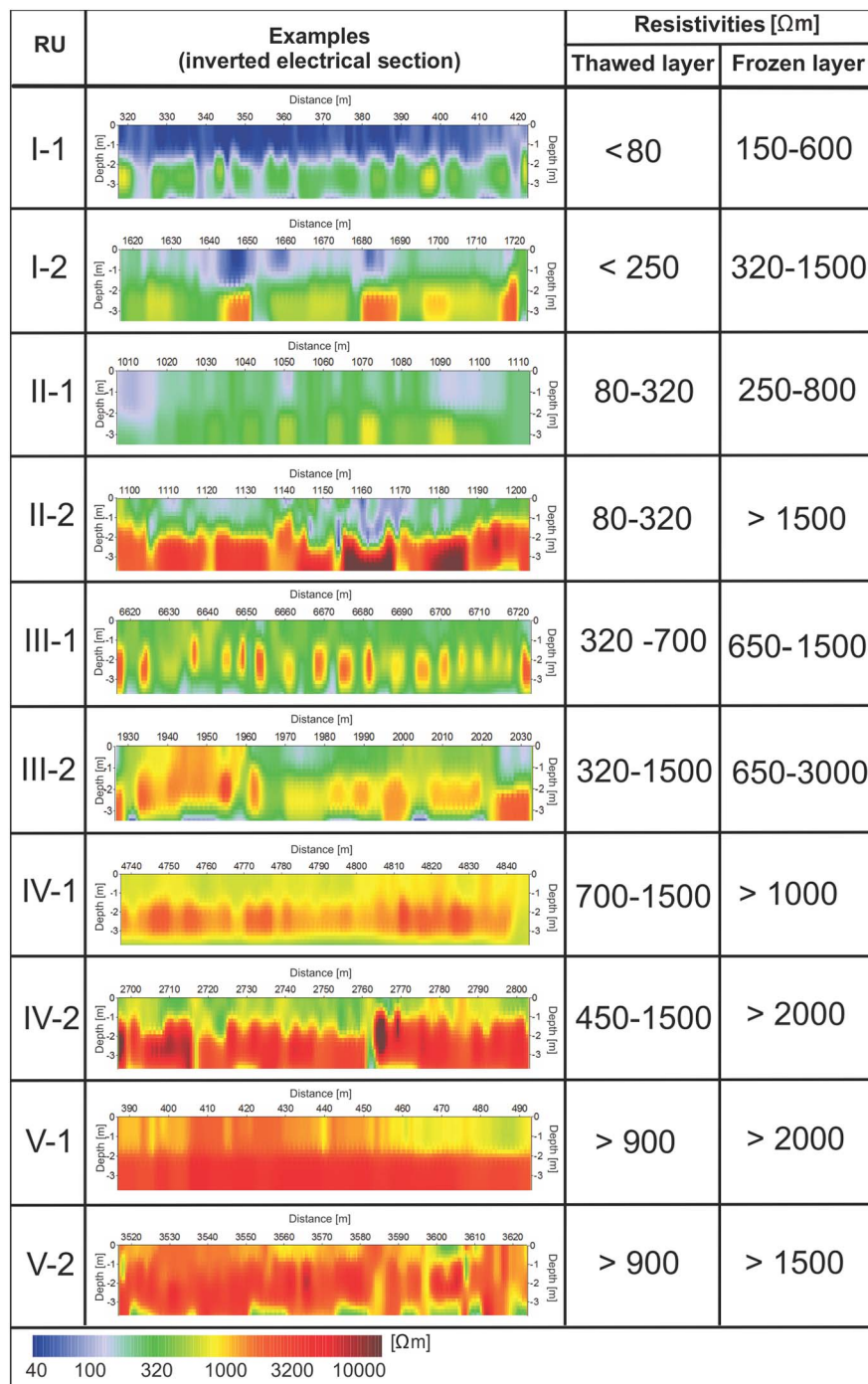


Fig. 5. Resistivity units (RU) based on the resistivity distribution in the active and permafrost layers.

puted from the resistivity increase in the CCR section, is hardly visible in the GPR section, but also sedimentary structures are missing. In contrast to GU Ila-2 (Fig. 7A) the GPR section of GU Iic-2 (Fig. 7B) shows subparallel low-amplitude reflections in the thawed layer and strong but discontinuous reflections below the thaw line. They are interpreted as caused by frozen gravel, which is confirmed by the drill core: below a top layer, consisting of silt and fine sand with isolated gravels, middle and coarse gravel are found at 0.7 m depth. Unlike the core of GU Iic-2 the core of the reflection-free GU Ila-2 indicates very fine-grained material such as clay and silt up to about 1 m depth. We assume that this relatively homogenous layer extends to a depth of at least 3.5 m, leading to a high attenuation of the GPR signal and to an almost reflection-free section.

5. Discussion and sedimentological interpretation

The CCR data, respectively RUs (Fig. 5), together with GPR pattern as well as grain size analysis from the core logs provided the basis for the geophysical classification resulting in 18 GUs (Fig. 10).

The 10 different RUs (Table 2) show a high variety of resistivities in the thawed and frozen layers because of the large differences of the resistivities of water and ice, respectively (Table 1). The resistivity of frozen soils ranges between 1000 and several 100,000 Ωm dependent on ice content, temperatures, and soil type; whereas unfrozen soils mainly have resistivities well below 1000 Ωm (Table 1). Consequently, we observe a pronounced resistivity increase in the frozen layer compared to the thawed top layer (Fig. 5). Only for high resistivities

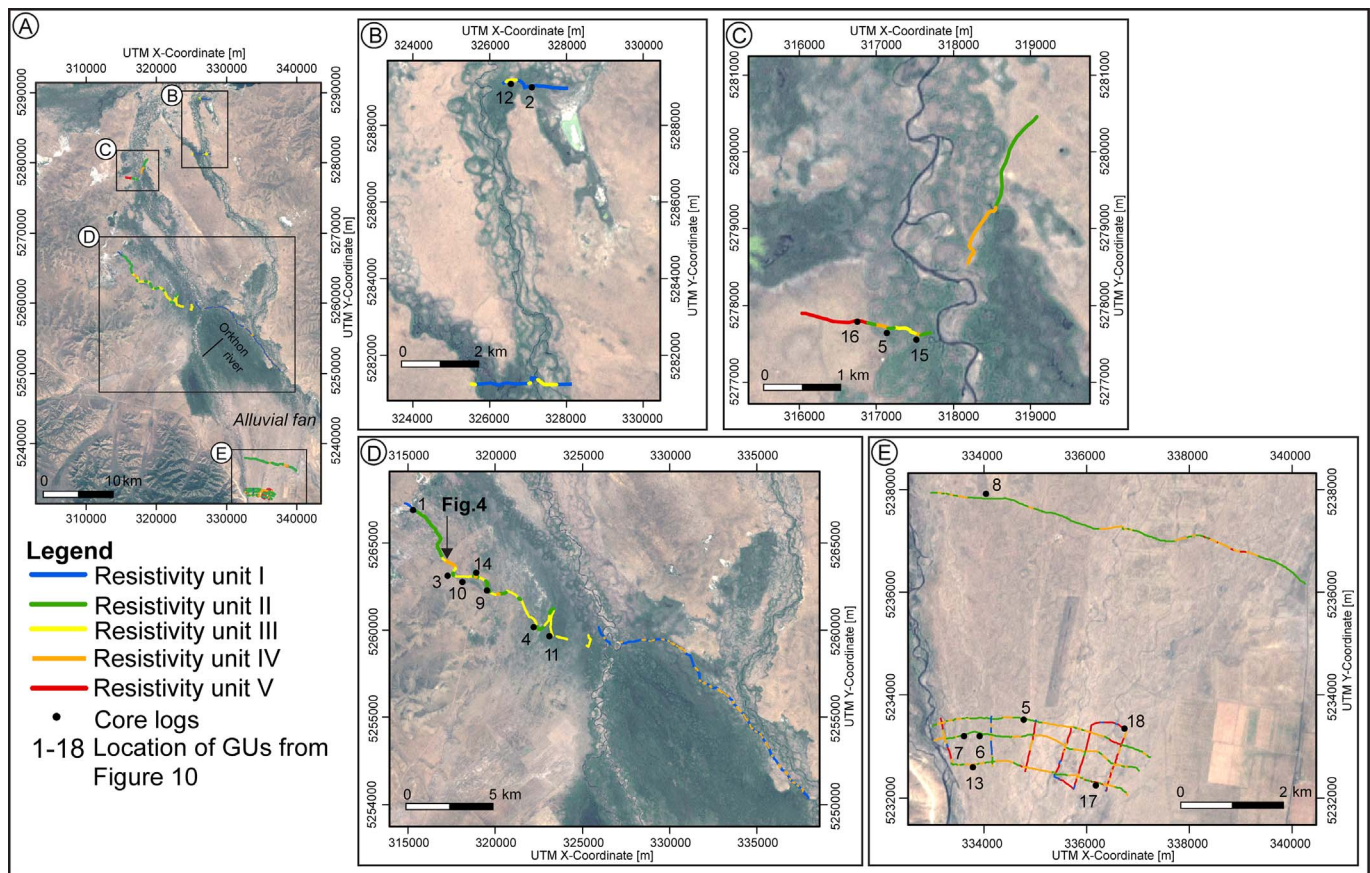


Fig. 6. Distribution of resistivity units RU I to RU V in the Orkhon Valley, location of the drill holes (black dots), and location of the 18 GPR sections shown in Fig. 10.

in the thawed layer, i.e., low water saturations, the resistivity of the frozen layer increases only moderately (cp. RUs IV and V in Fig. 5). However, also the resistivities of the frozen layer vary over a wide range. They depend on water content, temperature, and soil type. The soil type matters because water in soil can remain liquid at temperatures below the bulk water freezing point. The pore water freezing point decreases due to the Gibbs-Thomson effect with decreasing pore size or grain size, respectively. Therefore, frozen clay, silt, sand and gravel show a wide range of resistivities. The resistivity of unfrozen soils mainly depends on water content but also on porosity, water salinity, and cation exchange capacity (CEC). We assume that the water content of the thawed layer mainly depends on the water retention of the sediment (Table 1). We justify this (i) by assuming that the geophysical methods mainly image the vadose zone of the Orkhon Valley and (ii) by the low precipitation in the six months before our measurements (only 10% of the annual precipitation falls between November and May). Hence, we expect a decreasing resistivity with decreasing grain size related to the increasing water retention (Table 1) and CEC with decreasing grain size.

Based on our results, we found that one RU can have various GPR patterns depending on the distribution of liquid water and ice and on the type of sediment (Fig. 10). The latter is evident from core logs. The GPR data allow for identifying channel architectures (cp. Figs. 8 and 9); but elsewhere they are often characterised by low penetration depths because of the high content of fine-grained material and the associated low resistivity, confirmed by the CCR data (cp. Figs. 7 and 9).

The 18 GUs are now used for a sedimentological interpretation. The GUs from Fig. 10 can be differentiated into four different sedimentologies according to the grain size information derived from the related core logs: (i) predominant silt and fine sand, (ii) clay dominated sediments, (iii) coarse sand and gravel, and (iv) predominantly sand with isolated gravel (Table 2).

By comparing the resistivity sections with the drilling results we recognise that the frozen, high-resistivity layer often coincides with coarse-grained sediments such as coarse sand or gravel, i.e., often the resistivity boundary also represents a material boundary (cp. Figs. 7 and 10). The coincidence is caused by the reduced freezing point of the fine-grained sediments covering the coarse sediments—a fining-upward trend is observed in general in the Orkhon Valley. Moreover, the fine-grained deposits (clay, silt, fine sand) entail low resistivities in the upper horizon (cp. Fig. 7).

Sediments with different grain sizes are deposited by distinct transport mechanisms (e.g., Reading, 1996). Three different sedimentological processes are currently active in the Orkhon Valley, as described by various authors (Grunert et al., 2000; Lehmkuhl and Lang, 2001; Grunert and Lehmkuhl, 2004; Hülle et al., 2008): (i) fluvial sediment transport by the Orkhon River system, (ii) aeolian transport by wind with velocities of up to 22 m/s, and (iii) alluvial transport of unconsolidated sediments from the Khangai Mountains or from the river into the Orkhon Valley triggered by seasonal events.

In the following, the predominant sedimentary depositional environments will be discussed. We deduced them by carefully examining grain size distribution of the sediments and sediment texture visible in the cores. This classification combined with information from satellite images and field observations allows interpreting the different sediments as particular facies associations (Table 2).

5.1. Fluvial deposits

We distinguish fluvial sediments deposited by high- and low-energy flow which are characterised (i) by coarse sand and gravel with finer material like silt at the top, and (ii) fine sediments, such as clay and silt, respectively. Units GUs IVb-1, IIc-2, III-2, and IV-2 (Fig. 10) are interpreted as a coarse fraction deposited by high-energy flow. Typical

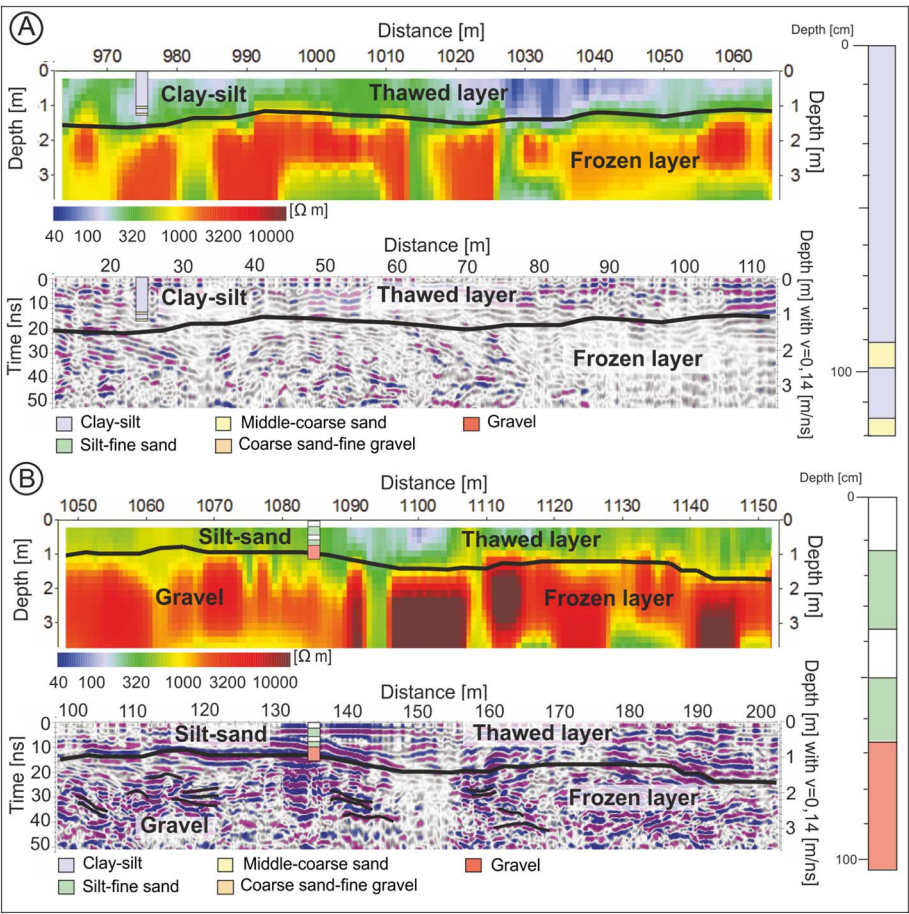


Fig. 7. CCR and GPR sections of RU II-2 with examples for (A) GU Ila-2 and (B) GU Ilc-2. The interpreted boundary between thawed and frozen layers is marked by the black line. While GU Ila-2 (A) and GU Ilc-2 (B) show similar resistivities, the GPR reflection patterns are different. The differences are caused by variable grain sizes and sediment deposits shown next to the geophysical sections. Note that the lower boundary of the permafrost layer exceeds the penetration depth and its lower limit therefore remains unknown.

Table 2
Assignment of geophysical units (GUs) to sedimentary classes and to sediment facies (for detailed information about geophysical units see Fig. 10).

Geophysical unit	Sedimentary classes	Interpretation (facies)	Sediment deposits
I-1	Predominantly silt and fine sand	Aeolian	Aeolian sediments
IIb-1			
IIIa-1			
I-2	Clay dominated sediments	Fluvial	Floodplain sediments
IIc-1			
Ila-2			
IIc-1			
IVb-1	Coarse sand and gravel		Channel sediments type 1
IIc-2			
III-2			
IV-2			
Vb-2		Alluvial	Channel sediments type 2
IIb-2			Channel sediments type 3
Va-2	Predominantly sand with isolated gravel		
Ila-1			Debris flow sediments
IIIb-1			
Iva-1			
V-1			

fluvial depositional GPR patterns such as steeply inclined reflections from gravel dunes (Fig. 8D) and well-defined channels with layers of finer material (silt to fine sand) mostly represent abandoned channels (Fig. 8A, B). The recognition of individual palaeochannels and the

determination of their dimensions allow for a reconstruction of the characteristics of the former river systems. The channel width/depth ratio is related to flow energy conditions and thus provides information on sediment transport processes. Here the width/depth ratio is relatively low so that the river mainly transports suspended load (Leeder, 1999), such as particles of fine sand, silt, and clay. If the river preferentially transports bedload sediments, the decreased bank stability results in a lower ratio (Figs. 8, 9). Coarse pebbles accumulate at the banks of high-energy channels. They originate from damaged levees or were deposited as bars. They occur close to the Orkhon and its former meanders. This kind of channel sediment is characterised by gravel beds with a thickness of at least 0.4 m, overlain by a 0.5 to 2.1 m thick layer of silt and fine sand and described as ‘type 1’ in Table 2.

The finer fluvial fraction consists of clay-dominated series as seen in GUs I-2, IIc-1, Ila-2, and IIc-1 (Fig. 10), which are interpreted as floodplain sediments (Fig. 8C) deposited in a low-velocity environment on both sides of the river.

5.2. Alluvial deposits

Alluvial deposits mostly show a heterogeneous composition controlled by the source region. Typical signatures are wide grain size spectra dominated by detritus in clayey-silty to coarse grain fractions (pebbles, boulders) within a finer matrix. This kind of deposition is visible in remnants of debris flows (Table 2). Such flows are triggered by intense rainfall, glacial melt, or a combination of both. They originate at the hillslopes of the Khangai Mountains. The flows are dominated by a coarse grain fraction but occasionally show fine to middle sands as observed in GUs Ila-1, IIIb-1, IVa-1, and V-1 (Fig. 10).

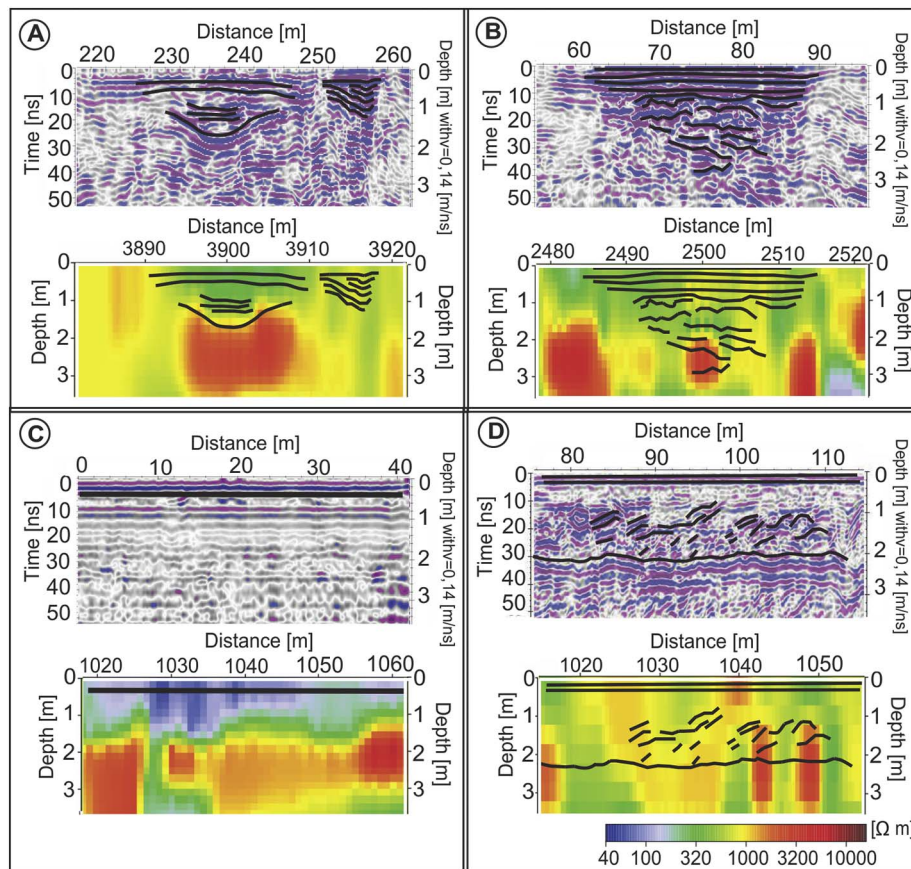


Fig. 8. Typical GPR features of fluvial sediments: (A) well-defined filled channel with fine sediments, ~15 m wide, (B) channel sediments overlain by horizontal bedded layers and a grass cover on top, (C) floodplain sediments characterised by strong attenuation of the GPR waves caused by fine-grained material, and (D) steeply inclined gravel dunes in a channel overlain by horizontally bedded layers.

We found them west of the Orkhon River close to the hillslopes (see cross sections A and B in Fig. 11A and B respectively).

Another form of alluvial deposits is related to the Orkhon River stream channel that widens in the alluvial fan at the northern foot of the Khangai Mountains. Sands with interbedded gravels, coarse sands or gravels compose the channel stream system of the alluvial fan. They constitute abandoned channels, main streams, former and younger channels, and remnants of the older fan surface. Based on grain size distributions, GPR patterns, and resistivity distributions we differentiate three channel types. Type 1, characterised as fluvial deposit, has been described above (cp. Section 5.1). Channel type 2 mainly consists of gravels as seen in GU Vb-2 (Fig. 10) and is found in the alluvial fan. These channel deposits only have a thin cover of fine sediments evidenced by high-amplitude GPR reflections without strong attenuation at the surface and the impossibility to penetrate them by percussion drilling. Channel type 2 also differs from type 1 regarding the

content of fine material, which is hardly found in channel type 2. Units GU I1b-2 and Va-2 (Fig. 10) are interpreted as channel type 3 dominated by sands with isolated gravels, which were deposited by low-energy streams.

5.3. Aeolian deposits

Aeolian deposits are typically well-sorted, fine-grained sediments with a maximal grain size of medium sands (up to 0.63 mm). We interpret GUs I-1, I1b-1, and IIIa-1 (Fig. 10), which exhibit a high content of fine material and are dominated by loess, as aeolian deposits. The loess is probably of Pleistocene age (Schwanghart and Schütt, 2008) and originates from the central Asia desert and steppe regions.

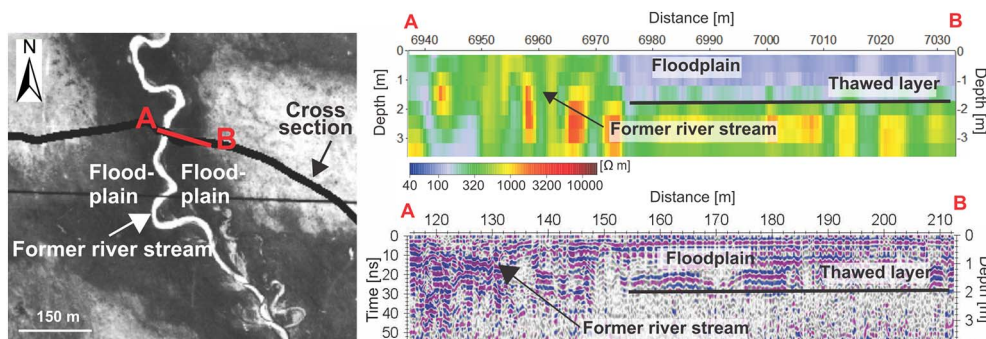


Fig. 9. Former river course as seen in Komsat imagery (left) and geophysical data along the profile between A and B (right).

RU	ρ [Ω m]	Reflection pattern	Description	Core logs	GU	Location nr of GU (Fig. 5)	RU	ρ [Ω m]	Reflection pattern	Description	Core logs	GU	Location nr of GU (Fig. 5)
I-1	< 80		strong attenuation, higher amplitude reflections	no core data	I-1	1	III-1	320-700		two clear horizontal reflections	no core data	IIIb-1	10
I-2	< 250		strong attenuation, lower amplitude reflections	no core data	I-2	2	III-1	320-700		strong attenuation, lower amplitude reflections	no core data	IIIc-1	11
II-1	80-320		clear horizontal reflection		IIa-1	3	III-2	320-1500		two clear horizontal reflections, downwards chaotic reflections	no core data	III-2	12
			strong attenuation, lower amplitude reflections		IIb-1	4	IV-1	700-1500		reflection free, partly discontinuous reflections, hyperbola		IVa-1	13
			strong attenuation, higher amplitude reflections		IIc-1	5	IV-1	700-1500		two clear horizontal reflections, inclined reflections		IVb-1	14
II-2	80-320		strong attenuation		IIa-2	6	IV-2	450-1500		strong attenuation, downwards chaotic reflections		IV-2	15
			strong attenuation, downwards chaotic reflections		IIb-2	7	V-1	> 900		reflection free		V-1	16
			clear horizontal reflection, chaotic and inclined reflections		IIc-2	8	V-2	> 900		reflection free	no core data	Va-2	17
III-1	320-700		discontinuous reflections, isolated hyperbola		IIIa-1	9	V-2	> 900		discontinuous high-amplitude reflections	no core data	Vb-2	18

Clay-silt Silt-fine sand Middle-coarse sand Coarse sand-fine gravel Gravel

Fig. 10. Assignment of geophysical units (GU) based on the resistivity units (RU), the GPR reflection pattern, and core log information. The shown GPR sections are 70 m wide and 5 m deep. Their locations are indicated in Fig. 6.

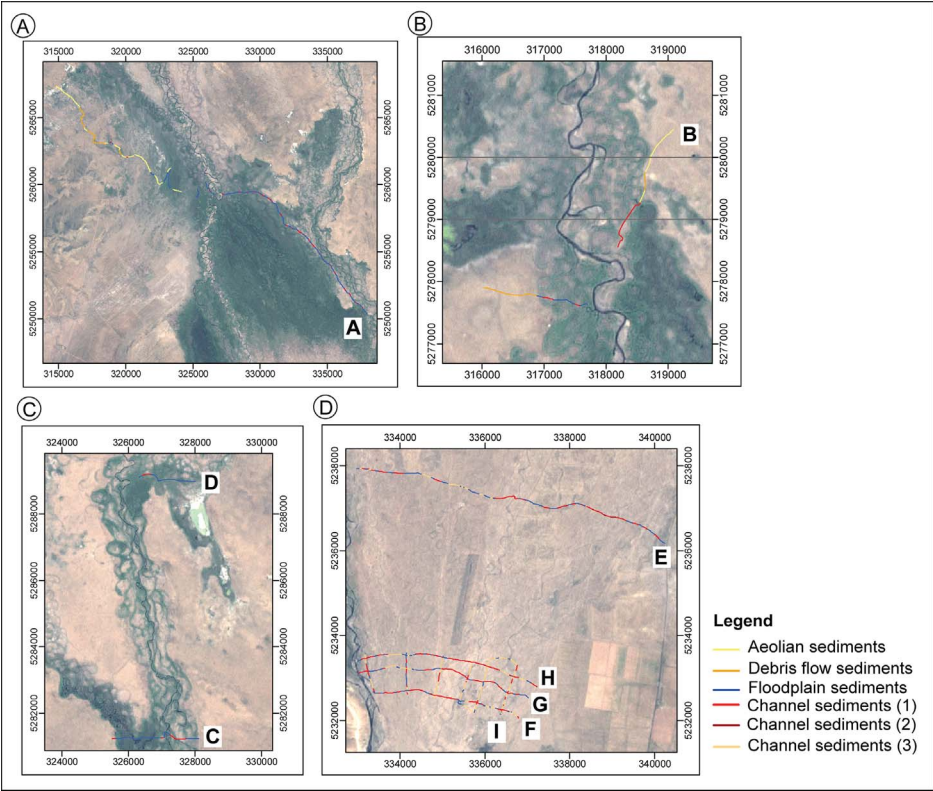


Fig. 11. Distribution of sediment deposits in the Orkhon Valley along our cross sections A to I. See Fig. 1 for location.

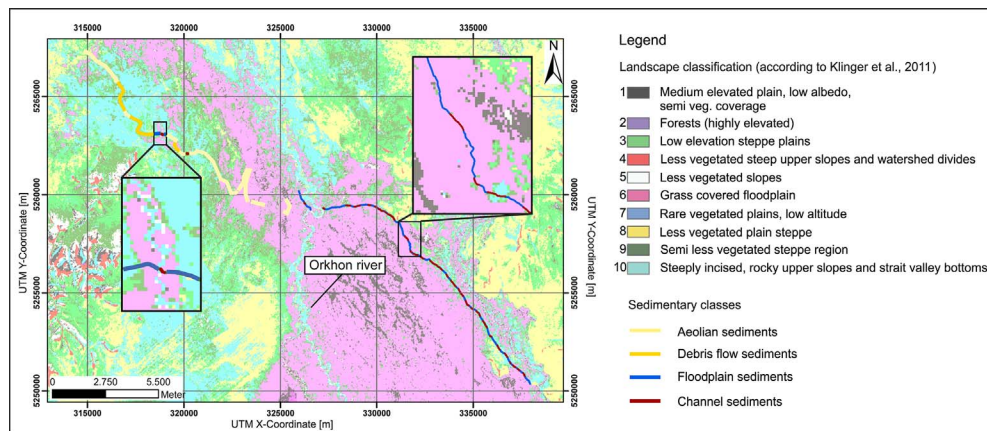


Fig. 12. Landscape classification by Klinger et al. (2011) compared to our sedimentological analysis.

5.4. Comparison to a landscape classification of the middle Orkhon Valley

Here, we compare our sedimentological interpretation of the geophysical surveys with a remote sensing based landscape classification that considers vegetation, elevation, albedo, and slope gradients. Klinger et al. (2011) used principal component analysis and fuzzy classification algorithms based on orthorectified ETM + satellite imagery and SRTM3 elevation data to obtain the landscape classification of the middle Orkhon Valley. For the comparison of our sediment deposits with their landscape classes, we overlay our results onto their maps (Figs. 12, 13). We notice that (i) fluvial units correspond to landscape classes that represent incised thalwegs and upper slopes; (ii) our fine-grained floodplain units are present in regions classified as grass-covered floodplains; (iii) alluvial units mainly occur where Klinger et al. (2011) mapped sparsely vegetated, flat steppe areas; and (iv) aeolian sediments are found in elevated steppe regions and in sparsely vegetated, flat steppe areas. In general, the predominant features of the middle Orkhon Valley are flat steppe areas in the west and a palaeochannel system in the east. Whereas our sedimentological interpretation mostly matches the landscape classes, we also observe inconsistencies. For example, the western side of profile A (Fig. 1 for location) was mainly classified as grass-covered floodplain, while our interpretation shows not only floodplain but also aeolian sediments (Fig. 12). For profile B (Fig. 1 for location), the landscape classification shows less vegetated plain steppe in the west and grass-covered floodplain in the east (Fig. 13). Our interpretation reveals that the plain steppe in the west consists of debris flow sediments. In the east, geophysical data confirm the floodplain sediments but additionally detect incised channels. The existence of one of these channels, i.e., a palaeoriver, is supported by a nearby archaeological site whose inhabitants apparently made use of the proximity to the fresh water source (Fig. 13; Grütznier et al., 2012).

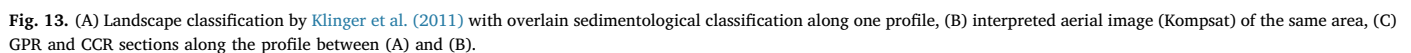
The comparison of our interpretation with the results of the landscape classification showed that a direct transfer between the two is hardly possible. First, Klinger et al. (2011) introduced more classes. Hence, our three main sedimentary deposits overlap with different landscape classes. Second, as the landscape classification approach is based on remote sensing data only, areas with similar morphology and the same surface cover will belong to the same landscape class even though different sediment facies are present beneath the surface. Thus, a loess-covered alluvial fan surface will hardly be distinguished from a loess-covered floodplain. Consequently, aeolian and alluvial deposits would belong to the same class. However, by comparing the results for the entire middle Orkhon Valley we find a quite good agreement between the landscape classification and the geophysical classification. Nevertheless, one should keep the ambiguities of remote sensing based classifications in mind when interpreting them (cf. Heiner et al., 2015).

6. Conclusions

We applied a methodology to study the shallow sediment architecture of a large basin, the middle Orkhon Valley, Mongolia, where fluvial, alluvial, and aeolian processes interact and result in a highly heterogeneous valley fill. The GPR and CCR were measured along selected cross sections to subsample representative areas. They span, with a total length of about 60 km, the entire valley. The geophysical data are calibrated with shallow drillings and outcrops. We classify the geophysical results into geophysical units, which we subsequently assign to four sedimentary classes. They are used for a process-orientated interpretation in terms of fluvial, alluvial, and aeolian deposits. By applying this interpretation, we image the former river course with its associated sediments and the floodplain and steppe areas. Aeolian silts and fine sands compose the steppe regions. Debris flow sediments originating from the surrounding slopes are deposited in the flat of the Orkhon Valley or found in incised depressions. Floodplain sediments accumulate in the wetlands of the river and channel sediments are found close to the Orkhon River (at former river courses) and on the alluvial fan. A comparison of our sedimentological interpretation with a remote sensing based landscape classification (by Klinger et al., 2011) showed, in general, a good match between both methods. Hence, our results can be extrapolated to the entire valley using remote sensing data. However, the comparison also revealed inconsistencies in terms of the sediment architecture. For example, areas entirely characterised as floodplains by the landscape classification are interrupted by several channels in the geophysically based interpretation. As these channels are often overlain by fine-grained sediments, the landscape classification only records the surface information and misses the channel sediments in the subsurface. As the landscape classification relies on surface parameters only, it is a mere snapshot of present surface characteristics. Thus, its validity in terms of sediment architecture is limited. In contrast to the landscape classification, the combination of geophysical methods and core logs takes subsurface information into account and allows a detailed differentiation of depositional environments and sedimentological processes. Thus, the sedimentological development within a particular geological time period can be recorded by the developed methodology.

This methodology can be applied to similar settings, not only in Mongolia, and allows determining the sediment distribution of vast areas with reduced effort. It closes the gap between one-dimensional drilling data and maps of surface properties obtained by remote sensing or satellite images by geophysical measurements. However, the methodology also has some implications when applied for sedimentological research especially in permafrost regions:

- CCR has proven to be valuable for large surveys as it has the advantage of covering long profiles in a relatively short time.



- GPR can reveal sedimentological architecture in great detail but is limited to shallow penetration depth especially for a high-conductive uppermost layer, which the thawed layer often is. We achieved much better results when the thaw line was close to the surface. Thus, we consider it beneficial for sedimentological research to carry the burden of working in cold conditions for the sake of higher GPR penetration depths.
- Drill cores, although naturally limited to very few locations, proved invaluable in establishing the geophysical classification and even more the sedimentological interpretation. This certainly limits the

- We characterised various channels and identified their spatial relocation in the Orkhon Valley, but for the purpose of this study we did not undertake any dating. However, for the chronological reconstruction of palaeoriver courses, age dating of the drilled channel sediments is required.

The geophysical data sets that our analysis is based on are published open access under: [doi.pangaea.de/http://dx.doi.org/10.1594/pangaea.2019.0001](https://doi.org/10.1594/pangaea.2019.0001)

PANGAEA.755563.

Competing interests

The authors declare that they have no conflict of interest.

Acknowledgements

This work was financed by the Federal Ministry of Education and Research (01UA0801C) (BMBF) project 'Geoarchaeology in the Steppes - Reconstruction of Cultural Landscapes in the Orkhon Valley, central Mongolia'. We are grateful to our students Jasmin Blomeyer and Sebastian Storandt who helped with the field work as well as to our colleagues from the Mongolian Academy of Science for their support. A special thank you goes to Birte Ahrens and Henny Piezonka who took the burden of organizing the field campaigns. We thank our Mongolian drivers who managed to keep the cars running in the most difficult terrain. Four anonymous reviewers and the editor, Richard Marston, helped to improve the manuscript and are gratefully acknowledged.

References

- Bemmann, J., Pohl, E., Schütt, B., Schwanghart, W., 2010. Archeological findings in the Upper and Middle Orkhon Valley and their geographical setup. In: Mongolian-German Karakorum Expedition. Wiesbaden, pp. 8.
- Bemmann, J., Ahrens, B., Grützner, C., Klinger, R., Klitzsch, N., Lehmann, F., Linzen, S., Munkhbayar, L., Nomguunsuren, G., Oczipka, M., Piezonka, H., Schütt, B., Saran, S., 2011. Geoarchaeology in the Steppe – first results of the multidisciplinary Mongolian-German survey project in the Orkhon Valley, central Mongolia. *Stud. Arch.* 30, 69–97.
- Bemmann, J., Lehnendorff, E., Klinger, R., Linzen, S., Munkhbayar, L., Oczipka, M., Piezonka, H., Reichert, S., 2014. Biomarkers in archaeology – land use around the Uyghur capital Karabalgasun, Orkhon Valley, Mongolia. *Præhist. Z.* 89 (2), 337–370.
- Brown, J., Ferrians Jr., O.J., Heginbottom, J.A., Melnikov, E.S., 1997. Circum-Arctic Map of Permafrost and Ground-ice Conditions. 45 USGS Publications, ER. <http://pubs.er.usgs.gov/publication/cp45>.
- Chen, A., Parsekian, A.D., Schaefer, K., Jafarow, E., Panda, S., Liu, L., Zhang, T., Zebker, H., 2016. Ground-penetrating radar-derived measurements of active-layer thickness on the landscape scale with sparse calibration at Toolik and Happy Valley, Alaska. *Geophysics* 81 (2), H9–H19.
- Cserkés-Nagy, Á., Sztanó, O., 2016. Millennial-scale climatic fluctuation in the fluvial record during MIS3: very high-resolution seismic images from NE Hungary. *Geomorphology* 274, 116–128.
- Daniels, J.J., Roberts, R., Vendl, M., 1995. Ground penetrating radar for the detection of liquid contaminants. *J. Appl. Geophys.* 33 (1–3), 195–207.
- Davis, J.L., Annan, A.P., 1976. Impulse radar soundings in permafrost. *Radio Sci.* 11 (4), 383–394.
- Davis, J.L., Annan, A.P., 1989. Ground-penetrating radar for high-resolution mapping of soil and rock stratigraphy. *Geophys. Prospect.* 3, 531–551.
- Eppelbaum, L.V., Kutasov, I.M., Pilchin, A.N., 2014. *Applied Geothermics*. Springer (751 p).
- Etzelmüller, B., Heggem, E.S.F., Sharkhuu, N., Frauenfelder, R., Käab, A., Goulden, C., 2006. Mountain permafrost distribution modelling using a multi-criteria approach in the Hövsgöl area, northern Mongolia. *Permafrost. Periglac. Process.* 17, 91–104. <http://dx.doi.org/10.1002/ppp.554>.
- Grunert, J., Lehmkühl, F., 2004. Aeolian sedimentation in arid and semi-arid environments of Western Mongolia. In: *Paleoecology of Quaternary Drylands*. 102, pp. 195–218.
- Grunert, J., Lehmkühl, F., Walther, M., 2000. Palaeoclimatic evolution of the Uvs Nuur Basin and adjacent areas (Western Mongolia). *Quat. Int.* 65 (66), 171–192.
- Grützner, C., Bemmann, J., Berking, J., Frechen, M., Klinger, R., Klitzsch, N., Linzen, S., Mackens, S., Oczipka, M., Piezonka, H., Reichert, S., Schneider, M., Schütt, B., 2012. Improving archaeological site analysis: a rampart in the Middle Orkhon Valley investigated with combined geoscience techniques. *J. Geophys. Eng.* 9, S70–S80.
- Grygar, T.M., Elznícová, J., Tůmová, Š., Faméra, M., Balogh, M., Kiss, T., 2016. Floodplain architecture of an actively meandering river (the Ploučnice River, the Czech Republic) as revealed by the distribution of pollution and electrical resistivity tomography. *Geomorphology* 254, 41–56.
- Hausmann, J., Steinle, H., Kreck, M., Werban, U., Vienken, T., Dietrich, P., 2013. Two-dimensional geomorphological characterization of a filled abandoned meander using geophysical methods and soil sampling. *Geomorphology* 201, 335–343.
- Heiner, M., Batsaikhan, N., Galbadrakh, D., Bayarjargal, Y., Zumbelma, D., Ariungerel, D., Evans, J., von Wenden, H., Kiesecker, J., 2015. Towards a national GIS model to map terrestrial ecosystems in Mongolia: a pilot study in the Gobi Desert Region. In: *Proceedings of the Trans-disciplinary Research Conference: Building Resilience of Mongolian Rangelands, Ulaanbaatar Mongolia*, 9–10 June, 2015, pp. 24–34.
- Hilbich, C., Hauck, C., Hoelzle, M., Scherler, M., Schudel, L., Völksch, I., von der Mühl, D., Mäusbacher, R., 2008. Monitoring mountain permafrost evolution using electrical resistivity tomography: a 7-year study of seasonal, annual, and long-term variations at Schilthorn, Swiss Alps. *J. Geophys. Res. Earth Surf.* 113 (F1).
- Hinkel, K.M., Doolittle, J.A., Bockheim, J.G., Nelson, F.E., Paetzold, R., Kimble, J.M., Travis, R., 2001. Detection of subsurface permafrost features with ground penetrating radar, Barrow, Alaska. *Permafrost. Periglac. Process.* 12 (2), 179–190.
- Hülle, D., Stolz, C., Felauer, T., Hemplemann, N., Hilgers, A., Grunert, J., Lehmkühl, F., Radtke, U., 2008. Reconstruction of aeolian and fluvial interaction in the Gobi Desert Southern Mongolia. In: *Schriftenreihe der Deutschen Gesellschaft für Geowissenschaften*. 60, pp. 337.
- IPA, 2017. International Permafrost Association. <http://ipa.arcticportal.org/publications/occasional-publications/what-is-permafrost> (last access: 2017-03-13).
- Ishikawa, M., Sharkhuu, N., Zhang, Y., Kadota, T., Ohata, T., 2005. Ground thermal and moisture conditions at the southern boundary of discontinuous permafrost, Mongolia. *Permafrost Periglac. Process* 16, 209–216.
- Jadamba, N., Grimmelmann, W., Kampe, A., 2003. Hydrogeological map of Mongolia 1:1.000.000 explanatory notes. In: *Geologisches Jahrbuch. BGR-Reihe, Reihe C* 69 (Hannover).
- Klinger, R., Schwanghart, W., Schütt, B., 2011. Landscape classification using principal component analysis and fuzzy classification: archaeological sites and their natural surroundings in Central Mongolia. *DIE ERDE-J. Geogr. Soc. Berlin* 142 (3), 213–233.
- Kneisel, C., 2006. Assessment of subsurface lithology in mountain environments using 2D resistivity imaging. *Geomorphology* 80, 32–44.
- Kneisel, C., Hauck, C., Fortier, R., Moorman, B., 2008. Advances in geophysical methods for permafrost investigations. *Permafrost. Periglac. Process.* 19, 157–178.
- Kuras, O., 2002. The Capacitive Resistivity Technique for Electrical Imaging of the Shallow Subsurface. (Doctoral Dissertation) University of Nottingham, Nottingham.
- Leeder, M., 1999. *Sedimentology and Sedimentary Basins*. Blackwell Science Ltd., (Ch. 17) pp. 307.
- Lehmkuhl, F., Lang, A., 2001. Geomorphological investigations and luminescence dating in the southern part of the Khangai and the Valley of the Gobi Lakes (Central Mongolia). *J. Quat. Sci.* 16, 69–87.
- Lehmkuhl, F., Hilgers, A., Fries, S., Hülle, D., Schlütz, F., Shumilovskikh, L., Felauer, T., Protze, J., 2011. Holocene geomorphological processes and soil development as indicator for environmental change around Karakorum, Upper Orkhon Valley (central Mongolia). *Catena* 87 (1), 31–44.
- Lehmkuhl, F., Hülle, D., Knippertz, M., 2012. Holocene geomorphic processes and landscape evolution in the lower reaches of the Orkhon River (northern Mongolia). *Catena* 98, 17–28.
- Mackens, S., Klitzsch, N., Grützner, C., 2011. Geophysical Mapping of the Sediment Architecture in the Orkhon Valley, Mongolia. *Rheinisch-Westfälische Technische Hochschule Aachen* <http://dx.doi.org/10.1594/PANGAEA.755563>.
- Martin, P., 2007. Environmental Review of the Land and Property in Rights Project in the Selenge River Basin, Mongolia. International Trip Report, Prepared in Cooperation with Millennium Challenge Corporation, USGS, Science for a Changing World. U.S. Department of the Interior, U.S. Geological Survey, Reston, Virginia.
- Neal, A., 2004. Ground penetrating radar and its use in sedimentology: principles, problems, and progress. *Earth Sci. Rev.* 66, 261–330.
- Neukirch, M., Klitzsch, N., 2010. How to invert capacitive resistivity (line electrode) measurements with DC inversion programs. *Vadose Zone J.* 9, 882–892. <http://dx.doi.org/10.2136/vzj2009.0164>.
- Pellicer, X.M., Gibson, P., 2011. Electrical resistivity and ground penetrating radar for the characterisation of the internal architecture of Quaternary sediments in the Midlands of Ireland. *J. Appl. Geophys.* 75 (4), 638–647.
- Reading, H.G., 1996. *Sedimentary Environments: Processes, Facies and Stratigraphy*, third ed. Blackwell Science Ltd, Oxford.
- Rey, J., Martínez, J., Hidalgo, M.C., 2013. Investigating fluvial features with electrical resistivity imaging and ground-penetrating radar: the Guadalquivir River terrace (Jaen, southern Spain). *Sediment. Geol.* 295, 27–37.
- Reynolds, J.M., 1997. Ground penetrating radar. In: Reynolds, J.M. (Ed.), *An Introduction to Applied and Environmental Geophysics*, first ed. Wiley, Chichester, pp. 681–749.
- Rösch, M., Fischer, E., Märkle, T., 2005. Human diet and land use in the time of the Khans—Archaeobotanical research in the capital of the Mongolian Empire, Qara Qorum, Mongolia. *Veg. Hist. Archaeobotany* 14, 485–492.
- Schennens, S., Troncke, J., Wetterich, S., Allroggen, N., Schwaborn, G., Schirrmeister, L., 2016. 3D ground-penetrating radar imaging of ice complex deposits in northern East Siberia. *Geophysics* 81 (1), WA195–WA202.
- Schick, P., 2002. Anwendung eines Zweikomponenten-Modells der pF-Kurve auf Strukturveränderungen in Böden. *Bautechnik* 2, 65–77.
- Schrott, L., Sass, O., 2008. Application of field geophysics in geomorphology: advances and limitations exemplified by case studies. *Geomorphology* 93, 55–73.
- Schwanghart, W., Schütt, B., 2008. Holocene morphodynamics in the Ugi Nuur basin, Mongolia—insights from a sediment profile and 1D electrical resistivity tomography. *Z. Geomorphol.* 52 (2), 35–55 (Supplementary Issues).
- Schwanghart, W., Möller, B., Schütt, B., 2008. Environmental characteristics of the Upper and Middle Orkhon Valley, Mongolia. In: Bemmann, J., Hüttel, H.G., Pohl, E. (Eds.), *Mongolian-German Qara Qorum-Expedition. FAKA (Forschungen zur Archäologie Ausseruropäischer Kulturen)*, Bonn.
- Sodnom, N., Yanshin, A.L., 1990. *Geocryology and Geocryological Zonation of Mongolia*. Digitized 2005 by Parsons M. A. 1990 National Snow and Ice Data Center/World Data Center for Glaciology, Digital Media, Boulder (last access: 2017-03-13).
- Timofeev, V.M., 1974. The Employment of Capacitively Coupled Sensors in Engineering and Geological Studies (in Russian). (Ph.D. thesis) University of Moscow, Moscow.
- Topp, G.C., Davis, J.L., Annan, A.P., 1980. Electromagnetic determination of soil water content: measurements in coaxial transmission lines. *Water Resour. Res.* 16, 574–582.
- Van Wijk, W.R., De Vries, D.A., 1963. Periodic temperature variations in a homogeneous soil. In: Van Wijk, W.R. (Ed.), *Physics of Plant Environment*. North Holland Publ. Co., Amsterdam.
- Woodward, J., Burke, M.J., 2007. Applications of ground-penetrating radar to glacial and frozen materials. *J. Environ. Eng. Geophys.* 12 (1), 69–85.
- Wu, T., Wang, Q., Watanabe, M., Chen, J., Battogtokh, D., 2009. Mapping vertical profile of discontinuous permafrost with ground penetrating radar at Nalaikh depression, Mongolia. *Environ. Geol.* 56 (8), 1577–1583.